AGU PUBLICATIONS

JGR

Journal of Geophysical Research: Solid Earth

RESEARCH ARTICLE
10.1002/2013JB010512

Key Points:
- Flexural stresses drive rapid rotation of normal faults from steep to shallow dips
- Rotation is most rapid in thin faulted layers and promotes longer fault life span
- Rotation shapes the global distribution of active normal fault dips

Correspondence to:
J.-A. Olive,
jaolive@mit.edu

Citation:
Olive, J.-A., and M. D. Behn (2014), Rapid rotation of normal faults due to flexural stresses: An explanation for the global distribution of normal fault dips, *J. Geophys. Res. Solid Earth*, *119*, 3722–3739, doi:10.1002/2013JB010512.

Received 15 JUL 2013
Accepted 13 MAR 2014
Accepted article online 20 MAR 2014
Published online 24 APR 2014

Rapid rotation of normal faults due to flexural stresses: An explanation for the global distribution of normal fault dips

Jean-Arthur Olive[1] and Mark D. Behn[2]

[1]Massachusetts Institute of Technology/Woods Hole Oceanographic Institution Joint Program in Oceanography, Cambridge, Massachusetts, USA, [2]Department of Geology and Geophysics, Woods Hole Oceanographic Institution, Woods Hole, Massachusetts, USA

Abstract We present a mechanical model to explain why most seismically active normal faults have dips much lower (30–60°) than expected from Anderson-Byerlee theory (60–65°). Our model builds on classic finite extension theory but incorporates rotation of the active fault plane as a response to the buildup of bending stresses with increasing extension. We postulate that fault plane rotation acts to minimize the amount of extensional work required to sustain slip on the fault. In an elastic layer, this assumption results in rapid rotation of the active fault plane from ~60° down to 30–45° before fault heave has reached ~50% of the faulted layer thickness. Commensurate but overall slower rotation occurs in faulted layers of finite strength. Fault rotation rates scale as the inverse of the faulted layer thickness, which is in quantitative agreement with 2-D geodynamic simulations that include an elastoplastic description of the lithosphere. We show that fault rotation promotes longer-lived fault extension compared to continued slip on a high-angle normal fault and discuss the implications of such a mechanism for fault evolution in continental rift systems and oceanic spreading centers.

1. Introduction

Normal faults are highly localized zones of brittle shear deformation that accommodate extension in the crust and lithosphere. Andersonian theory predicts that in an extensional system, normal faults will form with a dip angle of 60–65° [*Anderson*, 1951], corresponding to a coefficient of friction of 0.6–0.85 common for most rock types [*Byerlee*, 1978]. However, this prediction is not consistent with fault dips inferred from focal mechanisms of normal-faulting earthquakes large enough to rupture a representative portion of the fault plane. The global distribution of active fault dips resembles a Gaussian distribution centered on 45° and limited to angles between 20° and 65° [*Jackson and White*, 1989; *Thatcher and Hill*, 1991; *Collettini and Sibson*, 2001; *Yang and Chen*, 2008] with a few notable outliers at very low [*Abers*, 1991; *Abers et al.*, 1997] and very high [*Yang and Chen*, 2008] angles (Figure 1). A similar pattern of fault dips is observed at the scale of individual rift systems [*Jackson and White*, 1989].

One hypothesis to reconcile Andersonian theory with the observed distribution of fault dips is to assume a low coefficient of friction (< 0.3) associated with the presence of weak minerals (e.g., serpentine) [*Escartin et al.*, 1997] in the fault zone. This could account for faults initiating at dips closer to 50° but would not allow dips lower than 45° in an Andersonian stress field where the principal stresses are horizontal and vertical. Alternatively, accumulated elastic stresses in the faulted layer could cause significant deviation of the principal stresses from the horizontal/vertical [*Spencer and Chase*, 1989]. Such elastic stresses could arise from uncompensated surface or Moho topography and/or shear from an underlying viscous layer. Another possibility is that intermediate-dipping normal faults initiate as the reactivation of thrust faults under an Andersonian, extensional state of stress. While it is mechanically easiest to reactivate fault planes dipping at 60°, it is not significantly more difficult to reactivate planes dipping in the 40–80° range [*Collettini and Sibson*, 2001]. Although reactivation may be an important process in some continental rifts, it clearly does not apply to oceanic spreading centers where faulting occurs in newly formed lithosphere. Further, each of these mechanisms requires a specific set of conditions that relaxes the assumptions of Andersonian theory. It is therefore unclear to what extent these processes (or any combination of them) would be reflected in the dip distribution at the scale of both global and individual rifts. It has also been suggested that the 45° mode of the dip distribution corresponds to the dip of pressure-insensitive ductile shear zones beneath the seismogenic layer into which

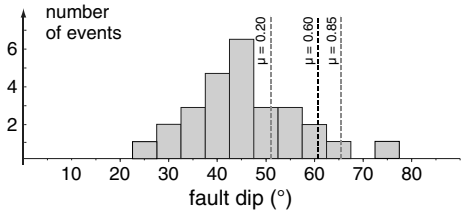

Figure 1. Dip distribution of 28 large ($M_w > 5$) dip-slip (rakes within 30° of downdip direction) normal fault ruptures (modified from *Yang and Chen* [2008]). Fault dips are inferred from focal mechanisms where local geology allows the nodal plane that likely corresponds to the rupture plane to be determined. Data from the compilation of *Jackson and White* [1989] and *Collettini and Sibson* [2001], complemented by data from *Abers et al.* [1997], *Abers* [1991] (low-dip end), and *Yang and Chen* [2008] (high-dip end).

faults root [*Thatcher and Hill*, 1991]. While this process may affect the dip distribution at all scales, it does not account for the spread of the distribution and is not well characterized from a mechanical perspective.

Another class of models that have been proposed to explain the observed distribution of fault dips argues that normal faults initiate at Andersonian angles of 60–65° but later rotate to shallower angles. One popular mechanism is a domino-style rotation of a set of parallel normal faults [*Proffett*, 1977; *Jackson and White*, 1989] down to a frictional lockup angle of ~30° [*Collettini and Sibson*, 2001] at which slip is no longer permitted, and a new set of steep faults forms to accommodate extension. In an Andersonian state of stress, slip on faults dipping <30° is only possible when fluid pressure exceeds the horizontal tensile stress. Such high fluid pressure is difficult to envision in settings where tensional stress promotes high permeability and drained conditions, which could explain why the observed range of normal fault dips is largely greater than 30°. However, the domino model is purely geometric and does not predict rotation rates or account for the possibility that a fault could become inactive before it reaches the lockup angle.

An alternative model for fault rotation involves isostatic adjustment of the footwall in response to tectonic denudation through plastic flow, resulting in low-angle detachment surfaces exposed as metamorphic core complexes [*Buck*, 1988; *Wernicke and Axen*, 1988]. A similar explanation has been put forward to explain low-angle detachments (or oceanic core complexes) found at slow- and ultraslow-spreading mid-ocean ridges and has been termed the "rolling hinge" model [*Buck*, 1988; *Lavier et al.*, 1999]. These models, which emphasize the effect of isostasy, are only valid for faults that have accommodated very large offsets (10–50 km) and explain the shallow dips of exposed fault surfaces rather than active fault planes. However, a recent numerical study of normal fault evolution [*Behn and Ito*, 2008] reported rotation of active fault planes from ~55° down to ~35° over less than 4 km of extension and prior to any rollover of the exhumed fault surface. More recently, *Choi and Buck* [2012] reported similar rotation in numerical simulations, which they attributed to flexural processes. They further proposed that flexural rotation of the active portion of detachment faults to shallower angles could lead to the formation of splay faults in the hanging wall, provided the detachment has retained sufficient strength. However, *Choi and Buck* [2012] did not investigate the physical mechanism by which flexure of the brittle layer leads to rotation of the active fault plane.

In this study, we present a simple mechanical framework for understanding rapid normal fault rotation after initiation at a high angle. We build on the classic finite extension theory of *Forsyth* [1992] and *Buck* [1993] and consider the effect of flexure on the optimal dip of a fault. Specifically, we derive the simplified energy budget of a growing fault and propose that fault rotation occurs in a way that systematically minimizes the external work required to sustain growth. We explore this hypothesis with a simple semianalytical model that first considers a purely elastic, infinitely strong faulted layer. This allows us to identify the key factors that control fault rotation kinematics and fault life span. We then incorporate a simplified treatment of plasticity in the semianalytical model to account for the finite strength of the lithosphere. In order to show that our simplified model captures the first-order physics of the system, we then compare our semianalytic results with more realistic 2-D geodynamic simulations of normal fault growth in an elastoplastic layer, which do not explicitly involve the assumption of "work minimization." Finally, we discuss applications of these models to fault evolution and the distribution of active fault dips in rift systems worldwide.

2. Work Minimization Model for Fault Rotation

Lithospheric flexure in response to slip on a normal fault has long been identified as a key mechanism to explain the topographical features of grabens and core complexes [e.g., *Vening-Meinesz*, 1950; *Buck*, 1988; *King et al.*, 1988]. It is therefore expected that the associated buildup of flexural stresses should feedback and influence subsequent fault evolution. *Forsyth* [1992] showed that flexure of a faulted layer due to finite offset

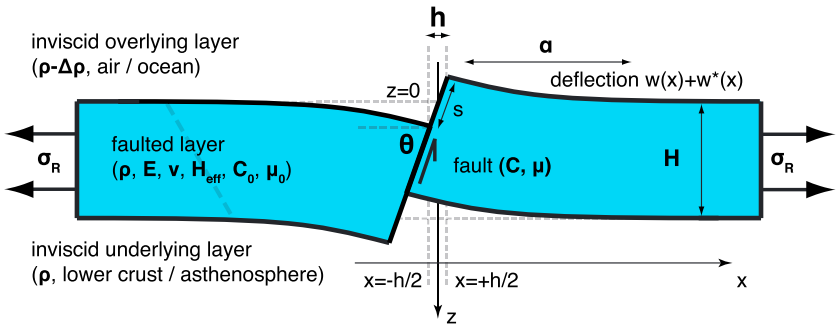

Figure 2. Schematic setup of our semianalytical model for fault evolution in an elastic/pseudoplastic layer. A far-field tensional stress, σ_R, drives extension along the fault (of heave h) and the associated deflection of the hanging wall and footwall blocks. The fault zone has a weak rheology characterized by a friction coefficient μ and cohesion C. Far from the fault, intact rocks (with μ_0, C_0) deform elastically or plastically with an effective elastic thickness H_{eff}. Slip on the fault ceases when σ_R becomes sufficient to break a new fault in intact rock.

on a normal fault acts to decrease its optimal dip (i.e., the dip that requires the least horizontal tension to keep the fault active) down to almost 30° after a few kilometers of extension. He showed that in order for a fault to remain active, horizontal tension must overcome frictional resistance as well as the buildup of topography and related flexural stresses. *Forsyth* [1992] proposed that faults would be abandoned when it becomes mechanically easier to break a new fault than to sustain slip on a preexisting fault. Using the assumption that fault dip does not change during growth, he concluded that only faults initiated at a shallow angle could accumulate large offsets because they would remain relatively close to their optimal dip during growth. This force balance model was later refined by *Buck* [1993] and *Lavier et al*. [2000], who treated the faulted layer as an elastoplastic rather than purely elastic thin plate. This assumption led to the prediction that normal faults would stay active longer when the faulted layer is thinner, in agreement with geological observations [*Lavier and Buck*, 2002]. However, like *Forsyth* [1992], these models did not explicitly consider the possibility that fault dip may readjust to the buildup of bending stresses, although the models of *Lavier et al*. [2000] did feature rotation of the shallowest portion of the active fault due to flexure. Here we present a mechanism by which flexural stresses could induce a rapid decrease in the dip of a growing fault and discuss its implications for fault life span. We propose that faults rotate in response to flexure of the footwall and hanging wall and do so in a manner that systematically minimizes the amount of work required to sustain slip on the fault.

Let us consider the energy balance on a growing normal fault, following the approach of *Cooke and Murphy* [2004]. We assume a fault of dip θ, which cuts through a layer of thickness H and accumulates a horizontal extension h (Figure 2). Far-field tensional forces supply mechanical work W_{EXT} to the system. This work can be related to the average tensional stress (σ_R) by

$$W_{\text{EXT}} = \int_0^h \sigma_R H \, dh \tag{1}$$

In order to sustain slip on the fault, the external work must overcome the frictional resistance along the fault surface (W_{FRIC}) and supply mechanical energy for bending the hanging wall and footwall (W_{INT}). In addition, work may be done against gravity (W_{GRAV}) as the fault creates topography, energy may be spent breaking new fault surface (W_{PROP}), and some work may be dissipated in the form of earthquakes (W_{SEIS}).

Since topography is modeled as the flexural readjustment of rigid displacement across a fault under gravity (see below and Appendix A), the work required to generate and sustain topography is included in W_{INT}, and we ignore all other sources of work done by or against gravity ($W_{\text{GRAV}} = 0$). Further, we assume that extension is accommodated on a single normal fault and that no new fault surfaces are formed as long as the fault is actively slipping. We can therefore neglect the energy cost of breaking intact lithosphere ($W_{\text{PROP}} = 0$). Lastly, the earthquake energy term (W_{SEIS}) integrates the drop in shear stress that occurs during each seismic rupture over many seismic cycles. This stress drop corresponds to a drop in fault strength that occurs when transitioning from static to dynamic friction. Overall, this term can be viewed as an intermittent dissipation of

Table 1. Summary of Notation and Values for Reference Parameters

Symbol	Definition	Value
H	Thickness of the faulted layer	
H_{eff}	Effective elastic thickness of the faulted layer ($\leq H$)	
h	Fault heave	
s	Fault offset	
L	Fault length	
ρ	Density of the faulted layer (and underlying layer)	2700–3300 kg m^{-3}
$\Delta\rho$	Density constrast between the faulted layer and the overlying fluid layer	2300–2700 kg m^{-3}
g	Gravitational acceleration	9.81 m s^{-2}
σ_R, σ_R^{BREAK}	Horizontal tensional stress needed to sustain faulting, horizontal tensional stress required to break a new fault in intact rock	
F_R	Horizontal tensional force needed to sustain faulting ($= H\,\sigma_R$)	
τ	Shear stress resolved on the fault	
σ_n	Normal stress resolved on the fault	
C, C_0	Cohesion of the fault zone, of the intact layer	
μ, μ_0	Friction coefficient in the fault zone, in the intact layer	
θ, θ_0	Dip of the fault, initial (optimal) dip of the fault	
E	Young's modulus	30–100 GPa
ν	Poisson's ratio	0.25–0.5
η_L	Viscosity of the faulted layer (in numerical model)	10^{24} Pa s
η_S	Viscosity of the ocean layer (in numerical model)	10^{17} Pa s
η_A	Viscosity of the asthenosphere (in numerical model)	10^{18} Pa s
U	Spreading half rate (in numerical model)	1 cm/yr
D	Flexural rigidity of the faulted layer	
α	Flexural wavelength of the faulted layer	
$w(x)$	Flexural response of the faulted layer due to offset on the fault	
$w^*(x)$	Topography of the faulted layer driven by rigid motion along the fault	
$w^T(x)$	Total topography induced by offset on the fault	
W_{INT}	Mechanical work done internally straining (bending) the faulted layer	
W_{FRIC}	Work done against friction on the fault	
W_{EXT}	Total external work supplied to the system = $W_{FRIC} + W_{INT}$	

a portion of the fault's frictional energy. Here we consider only a continuously growing fault that slips aseismically and neglect W_{SEIS}. We note, however, that if the fault grows by repeated earthquakes, its long-term averaged strength is perhaps best represented by its dynamic shear strength. This can be incorporated in our model by considering a lower friction coefficient in a continuously slipping fault.

The simplifying assumptions listed above yield the following work balance:

$$W_{EXT} = W_{FRIC} + W_{INT} \tag{2}$$

The frictional dissipation term is obtained by integrating shear stress multiplied by slip along the fault surface:

$$W_{FRIC} = \int_0^L \tau(l)s(l)\mathrm{d}l \tag{3}$$

By considering average stresses through the faulted layer and uniformly distributed slip on the fault plane, we can write

$$W_{FRIC} = \tau sL \tag{4}$$

where τ is shear stress, s is the fault offset ($h/\cos\theta$) and L is the fault length ($H/\sin\theta$). Slip on the fault is permitted as long as the Mohr-Coulomb criterion is met:

$$|\tau| = \mu|\sigma_n| + C \tag{5}$$

where μ is the coefficient of friction, σ_n is normal stress on the fault surface, and C is cohesion. A summary of notations is provided in Table 1. Assuming an Andersonian stress state and an average

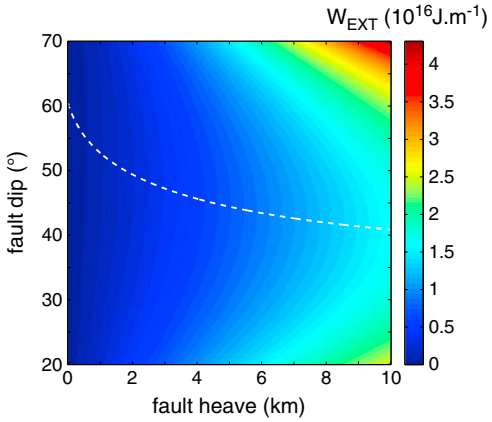

Figure 3. External work (W_{EXT}) required to keep a normal fault active as a function of fault dip and heave for increasing amounts of extension in a 10 km thick elastic (infinitely strong) layer. In our model, faults grow such that their dip evolves to shallower angles in order to minimize the increase in external work W_{EXT}. This corresponds to the lowest energy path represented by the white dashed line.

lithostatic stress of $-\rho gH/2$ in the faulted layer, the shear stress required for failure along the fault writes

$$\tau = \frac{C + \mu\rho gH/2}{\sin\theta\cos\theta + \mu\sin^2\theta}\cos\theta\sin\theta \tag{6}$$

The frictional energy dissipated along the fault is therefore written

$$W_{FRIC} = \frac{C + \mu\rho gH/2}{\sin\theta\cos\theta + \mu\sin^2\theta}Hh \tag{7}$$

The second component of work in equation (2) corresponds to the internal strain energy stored in the faulted layer as the footwall and hanging wall are bent upward and downward, respectively. W_{INT} is defined as the integral of stress multiplied by strain over the faulted layer:

$$W_{INT} = \int_V \frac{1}{2}\sigma_{ij}\epsilon_{ij}\,dV \tag{8}$$

To estimate W_{INT}, we first treat the faulted layer as a thin elastic plate of thickness H with Young's modulus E and Poisson's ratio ν, overlying an inviscid fluid half-space of the same density [*Buck*, 1988, 1993; *Forsyth*, 1992] (Figure 2). The density contrast between the layer and the overlying fluid (air or ocean) is $\Delta\rho$. This simplifying assumption allows us to relate W_{INT} to the deflection of the footwall and hanging wall blocks $w(x)$:

$$W_{INT} = \frac{1}{2}\int_{-\infty}^{+\infty} D\left(\frac{\partial^2 w}{\partial x^2}\right)^2 dx \tag{9}$$

where D is the flexural rigidity of the faulted layer,

$$D = \frac{EH^3}{12(1-\nu^2)} \tag{10}$$

The plate deflection resulting from slip on the fault is modeled by adding the contribution of (a) rigid motion of the hanging wall and footwall blocks along the fault and (b) flexure of the footwall and hanging wall blocks in response to gravity [*Weissel and Karner*, 1989]. If $w^*(x)$ denotes the topography resulting from step (a) alone, the deflection $w(x)$ corresponding to step (b) can be calculated as the flexural response to the load exerted by $w^*(x)$. This is achieved by solving the thin plate equation,

$$D\frac{d^4w}{dx^4} + \Delta\rho g w = -\Delta\rho g\, w^*(x) \tag{11}$$

The final topography resulting from steps (a) and (b) is simply $w^T(x) = w^*(x) + w(x)$. Details of the solution method are given in Appendix A. Specifically, we show that W_{INT} can be written as

$$W_{INT} = \frac{D}{16\alpha}\tan^2\theta\,\Psi\left(\frac{h}{\alpha}\right) \tag{12}$$

where α denotes the flexural wavelength of the faulted layer

$$\alpha = \left(\frac{4D}{\Delta\rho g}\right)^{\frac{1}{4}} \tag{13}$$

and $\Psi(y)$ is a dimensionless function described in Appendix A.

Combining equations (7) and (12), we now have an expression for the frictional and flexural work components as a function of fault heave and dip (see Appendix B for details and function definitions).

$$W_{EXT} = \underbrace{A_F(\theta)R_F(h)}_{W_{FRIC}} + \underbrace{A_I(\theta)R_I(h)}_{W_{INT}} \tag{14}$$

We then postulate that flexure acts to rotate the active fault plane such that the energy required to sustain extensional deformation is minimized. In other words, fault dip evolves to minimize the increase in tensional

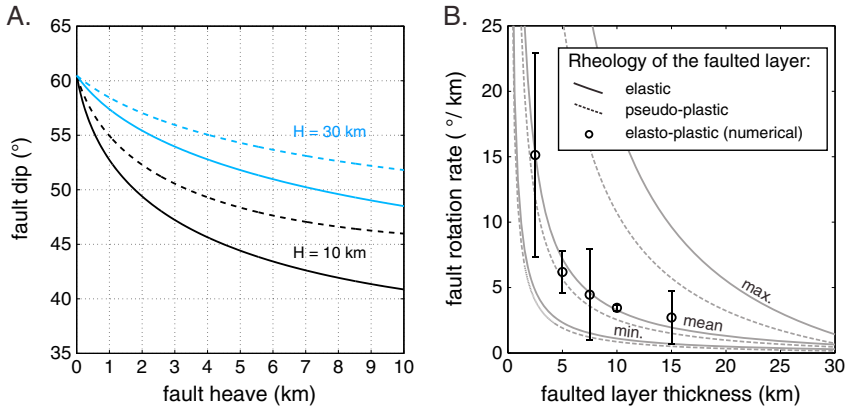

Figure 4. (a) Dip evolution of a normal fault cutting through a 10 km (black) and 30 km (blue) thick faulted layer that is either elastic (lines) or pseudoplastic with $H_{eff}/H = 0.5$. (b) Rate of fault rotation immediately following initiation (maximum), at $h = H/2$ (minimum) and averaged between these two stages, as calculated in our semianalytical elastic (lines) and pseudoplastic model ($H_{eff}/H = 0.5$, dashed lines) and measured from our numerical elastoplastic model (open symbols). For the numerical runs the symbols show the mean rate; error bars indicate maximum and minimum rotation rates.

work (W_{EXT}) with increasing extension (Figure 3). In mathematical terms, fault dip can be determined for a given amount of extension by the constraint

$$\frac{\partial}{\partial\theta}\left(\frac{\partial W_{EXT}}{\partial h}\right) = 0 \tag{15}$$

In the framework of the *Forsyth* [1992] force balance model, this is equivalent to allowing faults to rotate toward their optimum dip angle. Combining equations (14) and (15) allows us to formulate a nonlinear differential equation that we solve with a fourth-order Runge-Kutta method (Appendix B). The initial fault dip, θ_0, is assumed optimal with respect to an Andersonian stress field and therefore only depends on the coefficient of friction of the host rock:

$$\theta_0 = \frac{\pi}{2} - \frac{1}{2}\tan^{-1}\left(\frac{1}{\mu_0}\right) \tag{16}$$

The θ_0 is necessarily greater than 45° and is equal to ~60° and ~65° for $\mu_0 = 0.6$ and 0.85, respectively (Figure 1). We can then calculate fault dip as well as the various work terms as a function of increasing heave. The average horizontal tension that drives extension on the fault can also be obtained from equation (1):

$$\sigma_R = \frac{1}{H}\frac{\partial W_{EXT}}{\partial h} \tag{17}$$

A fault is abandoned when σ_R becomes greater than σ_R^{BREAK}, the stress required to break a new fault in intact lithosphere (friction μ_0, cohesion C_0) [*Forsyth*, 1992]:

$$\sigma_R^{BREAK} = \frac{C_0 + \mu_0 \rho g H/2}{\sin\theta_0 \cos\theta_0 + \mu_0 \sin^2\theta_0} \tag{18}$$

In all our calculations, we assume a cohesionless active fault plane and focus on the effects of changing fault zone friction and faulted layer thickness.

3. Semianalytic Results for Fault Rotation

3.1. Elastic (Infinitely Strong) Faulted Layer

The work minimization hypothesis results in a rapid rotation of faults from steep to intermediate angles, which constitutes the lowest energy path for the system (Figure 3). The rotation rate (degrees per kilometer of horizontal offset) is fastest immediately after fault initiation and subsequently decreases (Figure 4). For example, a fault with a friction coefficient of 0.6 cutting a 10 km thick elastic layer will rotate from 60° down to 45° over $<$ 5 km of horizontal extension. Further rotation down to 40° occurs over the next ~5 km of extension

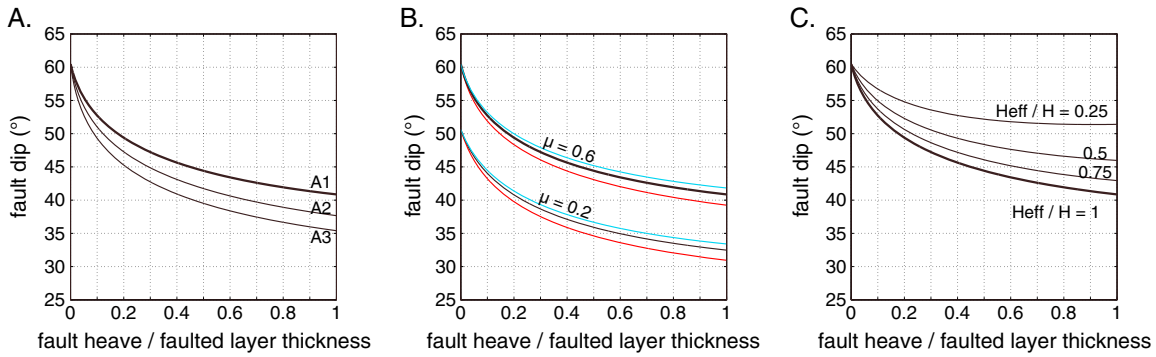

Figure 5. Evolution of fault dip as a function of accumulated horizontal offset (h) normalized by the faulted layer thickness (H) calculated from our semianalytical model. (a) Effect of changing the stiffness (E, ν) and density constrast $\Delta\rho$ of a 10 km thick layer. A1: default case, $E = 30$ GPa, $\nu = 0.5$, $\Delta\rho = 2300$ kg m^{-3}. A2: $E = 150$ GPa, $\nu = 0.25$, $\Delta\rho = 2300$ kg m^{-3}. A3: $E = 150$ GPa, $\nu = 0.25$, $\Delta\rho = 2700$ kg m^{-3}. (b) Effect of changing fault friction with parameters from case A1. The blue, black, and red curves correspond to $H = 15$, 10, and 5 km respectively. (c) Effect of pseudoplasticity in a 10 km thick layer with parameters from case A1. The ratio H_{eff}/H is indicated next to each curve.

(Figure 4a). Greater density contrasts between the faulted layer and the overlying fluid layer, as well as stiffer elastic moduli, lead to faster rotation (Figure 5a) down to about 35° after 10 km of extension.

We find that the average fault rotation rate (measured between $h = 0$ and $h = H/2$) scales as the inverse of the faulted layer thickness (Figure 4b, "mean" line). Consequently, the total amount of rotation experienced by a fault depends directly on its heave normalized by the thickness of the faulted layer (Figure 5). While the exact functional form of this dependence is not fully resolved here, it appears stronger than the sensitivity to the elastic parameters of the layer and to the density contrast with respect to the overlying fluid layer (Figure 5a). Due to this effect, faults that cut and flex a 30 km thick brittle layer will never undergo rotation rates greater than 2°/km of heave and will therefore retain dips close to their initiation angles over a comparable amount of extension (Figure 4). Further, although the friction coefficient assumed for the fault zone sets the initiation angle of the fault, it has very little influence on the total amount of rotation experienced after a given amount of extension (Figure 5b). Low-friction faults may therefore reach angles as low as 20–25° but only because they initiated at a lower angle.

Fault rotation in response to the accumulation of flexural stresses naturally affects the force balance on the growing normal fault. Allowing faults to rotate toward their optimum dip limits the increase in horizontal tension σ_R that would occur at a fixed dip (Figure 6a). In some cases fault rotation ensures that σ_R does not exceed the stress required to break a new fault in intact rock, thereby promoting unlimited fault growth. This effect dominates in thin brittle layers where fault rotation is rapid (Figure 6a, $H = 5$ km case). In a thicker layer, fault rotation is slower and stresses accumulate faster, leading to fault abandonment and the creation of a new fault after moderate amounts of extension (Figure 6a, $H = 15$ km case). By contrast, when fault rotation is ignored in the force balance calculation for an elastic plate, fault life span increases very slightly with brittle layer thickness [e.g., *Shaw and Lin*, 1996].

3.2. Elastic/Pseudoplastic Faulted Layer

So far, we have only considered a purely elastic faulted layer in which tensional stresses can accumulate without limitation. A more realistic description of the lithosphere must involve a finite yield strength that acts as a maximum allowable stress and promotes diffuse plasticity that locally weakens the layer at large stress/strains. Below we incorporate this mechanism into our semianalytical model in a highly simplified manner to qualitatively estimate its effect on fault rotation and life span.

We incorporate (pseudo) plasticity by replacing the true faulted layer thickness H by a lower effective elastic thickness $H_{eff} \leq H$ in all the terms related to W_{INT}. We use H_{eff} in equations (10) and (13) to define an effective flexural rigidity D_{eff} and an effective flexural wavelength α_{eff}. These parameters act as a crude measure of the amount of distributed plastic deformation that effectively weakens the faulted layer. In reality H_{eff} is spatially variable, and a direct function of plate curvature and the assumed yield strength envelop [*Buck*, 1988]. H_{eff} will be smallest in the regions of highest curvature because these regions represent the areas that have accumulated the greatest flexural stresses. In low-curvature regions, H_{eff} likely retains a value close to H. In

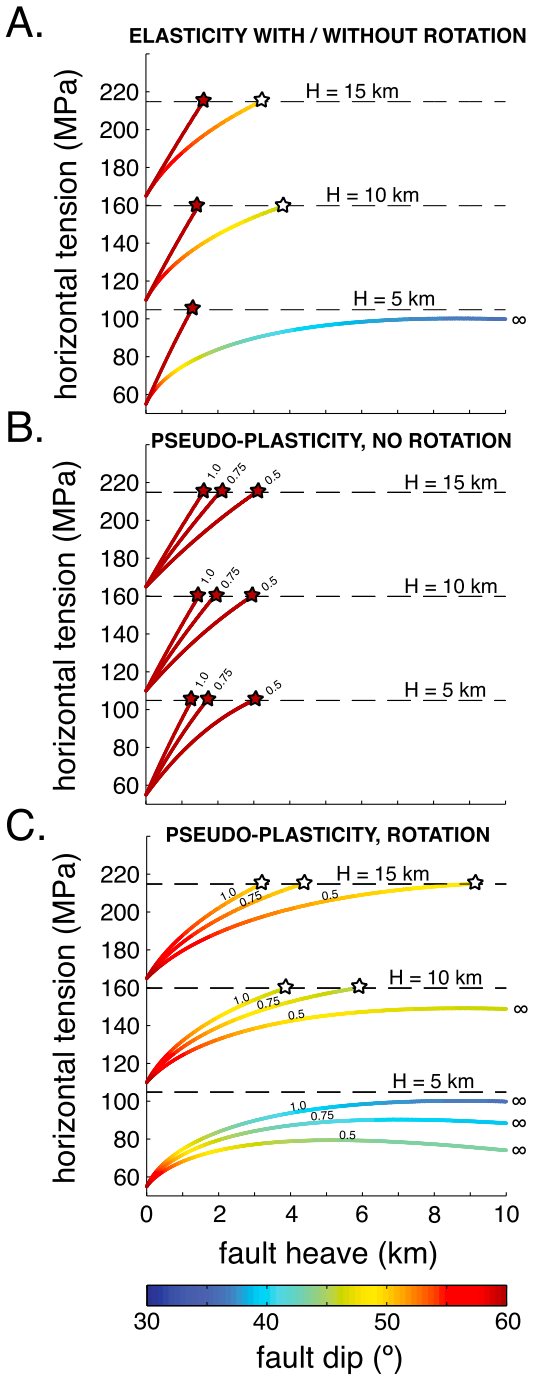

Figure 6

Ito, 2008]. In cases where faults are allowed to rotate (Figure 6c), pseudoplasticity complements the effect of rotation in promoting even longer fault life span in thinner layers.

Our semianalytical approach makes important predictions for dip evolution and fault life span. It is, however, limited by underlying assumptions that include (1) the thin plate approximation for calculating our simplified approach, we use a single H_{eff} value for the entire faulted layer, which represents an average effective thickness over a distance roughly equivalent to the (reduced) flexural wavelength of the plate. This approach clearly overestimates the amount of weakening due to plasticity, but it enables us to illustrate the first-order effects with the least amount of additional parameters.

The main effect of pseudoplasticity is to slow down fault rotation with respect to the elastic case. In a 10 km thick faulted layer with an effective elastic thickness of 5 km, a fault will only rotate down to ~50° after 4 km of extension, as opposed to ~45° in the purely elastic end-member (Figure 4a). For a given value of H, reducing the ratio H_{eff}/H leads to even slower rotation. This effect appears to hold over the entire range of H (Figure 4b). For a given H_{eff}/H, rotation rates in a pseudoplastic faulted layer scale as the inverse of the true layer thickness, which is the same as in the elastic end-member case.

Figures 6b and 6c illustrate the effect of pseudoplasticity on fault life span. In cases where faults are not allowed to rotate, a lower H_{eff}/H promotes longer fault life span by limiting the buildup of tensional stresses. Interestingly, for a given H_{eff}/H, fault life span appears almost insensitive to the true faulted layer thickness H. However, due to complex feedbacks between inelastic deformation and plate curvature, plastic weakening tends to be stronger in thinner (true thickness H) plates. In other words, H_{eff}/H will achieve lower values in plates that have a smaller initial H [e.g., *Buck*, 1988]. This effect is likely responsible for the classic prediction of longer fault life span in thinner faulted layers [*Buck*, 1993; *Lavier et al.*, 2000; *Lavier and Buck*, 2002; *Behn and*

Figure 6. Horizontal tension needed to sustain slip on a growing normal fault calculated as a function of accumulated heave, for various faulted layer thicknesses H, from our semianalytical model of fault growth in a thin, elastic/pseudoplastic layer. The multicolored curves correspond to cases where fault rotation is allowed to minimize the regional horizontal stress. Colors indicate the evolving fault dip. For comparison, dark red curves show stress increase in cases where fault rotation is not allowed and dip is held constant at 60°. The stars mark the amount of horizontal extension that can be accommodated before it becomes easier to break a new fault in intact lithosphere (requiring a stress shown as horizontal dashed lines) than to sustain slip on the active fault. The infinity symbols indicate cases where faults can grow indefinitely. (a) Elastic faulted layers. (b) Pseudoplastic layers without rotation. The ratio H_{eff}/H is indicated next to each curve. (c) Pseudoplastic layers with rotation.

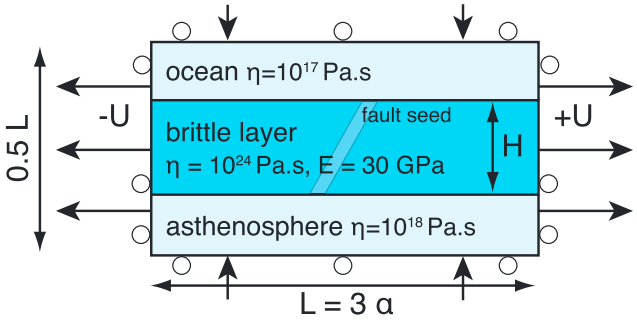

Figure 7. Schematic setup of our numerical models for fault evolution in an elastoplastic layer. The faulted layer is forced to be effectively elastic by setting the viscosity to be sufficiently large that the Maxwell timescale greatly exceeds the numerical time step chosen to integrate elastic stresses. Plasticity is implemented following a Mohr-Coulomb criterion. The fault is seeded at the first time iteration as a thin band of low-cohesion material dipping at the optimal initiation angle (equation (16)) and then allowed to evolve freely as strain localizes on this narrow shear band. See text for details.

W_{INT}, (2) a simplified treatment of plasticity, and (3) the hypothesis that rotation acts to minimize the increase in W_{EXT}. Therefore, to test validity of this approach, we compare our semianalytical results with more complex numerical simulations of normal fault growth based solely on conservation of mass and momentum, which do not incorporate any of the assumptions made thus far.

4. Numerical Models of Fault Rotation in an Elastoplastic Layer

In this section, we compare our semianalytical elastic results with numerical simulations of fault growth in an elastoplastic brittle layer. We solve for conservation of mass and momentum in a 2-D domain using the finite difference/particle-in-cell technique [*Harlow and Welch*, 1965] described by *Gerya* [2010]. Our model setup (Figure 7) involves a brittle layer of thickness H, viscosity $\eta_L = 10^{24}$ Pa s, Young's modulus $E = 30$ GPa, and Poisson's ratio $\nu = 0.5$. The brittle layer is situated between a low-viscosity asthenosphere ($\eta_A = 10^{18}$ Pa s) below and a low-viscosity "sticky ocean" layer ($\eta_S = 10^{17}$ Pa s) [*Crameri et al.*, 2012] above. The asthenosphere and ocean layers have thicknesses similar to that of the brittle layer. The ocean layer has a density of 1000 kg m^{-3}; the brittle and asthenospheric layers have densities of 3300 kg m^{-3}. To insure that flexure is not influenced by the model boundaries, the width of the box is set to 3 times the (elastic) flexural wavelength of the brittle layer (equation (13)). The height of the box is equal to 50% of its width. We pull on each side of the model domain at a half rate, U, and compensate the horizontal outflow of ocean and rock by imposing a matching inflow of material through the top and bottom boundaries, respectively. Shear tractions are set to zero on all boundaries.

The brittle layer behaves as an elastic-plastic solid while the other layers are effectively viscous. Elasticity is implemented following *Moresi et al*. [2003]. We impose a Maxwell viscoelastic rheology law in which the time derivative of the stress tensor is discretized with a backward finite difference scheme. This allows us to rewrite the rheological law as a simple viscous law with an effective viscosity that incorporates the elastic moduli and the time step chosen for the stress approximation (termed "computational time step" in *Gerya* [2010]). The terms related to the stresses from the previous iteration then appear in the discretized momentum conservation equation. The computational time step is chosen such that the effective viscosity vanishes in the high-viscosity (η_L) brittle layer, allowing the terms related to past stresses to dominate the momentum equation rendering the layer effectively elastic.

Plastic failure follows the Mohr-Coulomb criterion (equation (5)) with a friction coefficient of 0.6. Strain localization is promoted by decreasing the cohesion (initially $C_0 = 100$ MPa) linearly with the accumulated plastic strain [*Lavier et al.*, 2000]. The cohesion in intact material is $C_0 = 100$ MPa. We chose such a high value to promote longer fault life span (σ_R^{BREAK} is high), allowing us to follow the growth of a single fault over longer timescales before a new fault breaks, while still promoting diffuse plastic yielding in the footwall and hanging wall. Once a critical plastic strain corresponding to 250 m of fault offset is exceeded, cohesion is kept at a minimum value of 0.01 MPa. To initialize strain localization on a single normal fault at the beginning of each model run, we impose a rectangular "fault seed" of dip θ_0 (equation (16)) and width equal to 3 cell diagonals in the middle of the model domain. In this narrow region, plastic strain is set to the critical value and the cohesion is decreased accordingly. The grid resolution close to the fault is refined to about 500×500 m or less, which enables a mature fault width that is typically less than 2 km. A "healing" mechanism is implemented in the code to promote strain localization [*Lavier et al.*, 2000]. This consists in reducing the accumulated plastic strain by a small amount at every time iteration. In regions of diffuse plastic yielding the

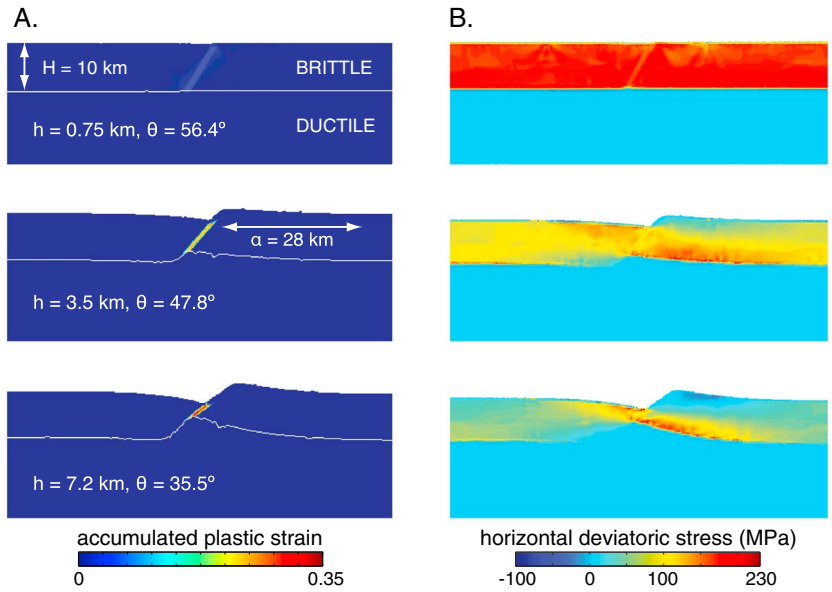

Figure 8. Snapshots of (a) accumulated plastic strain and (b) horizontal deviatoric stress (σ_{xx}') for various amounts of extension in numerical models of fault growth in a 10 km thick elastoplastic layer. Strain is highly localized into a < 2 km wide shear zone that represents the fault. The white line marks the brittle-ductile transition (base of the faulted layer).

accumulated strain and associated weakening heals within ~10,000 years but keeps building up in regions of localized deformation (i.e., shear zones). Once all the extensional strain has effectively localized on the fault (which usually takes less than 4 time iterations), we measure the average fault dip as a function of fault heave by visually fitting a line to the region of greatest accumulated plastic strain. Fault heave is estimated as the horizontal distance between the bottom of the hanging wall trough and the top of the footwall shoulder.

We ran five simulations spanning brittle layer thicknesses of $H = 2.5$ to 15 km. In each simulation the fault rotated rapidly from its prescribed initiation angle (60°) down to angles as low as 35° at rates comparable to those inferred from the simple work minimization models (Figures 8 and 9). Flexural stresses build up in the footwall and hanging wall and quickly saturate at the yield stress (Figure 8b) resulting in diffuse yielding within about half a flexural wavelength from the fault. We fit the dip versus heave curves measured in each simulation between $h = 0$ and $h = H/2$ with a second-order polynomial and measured the average slope of the polynomial to determine a smooth estimate of the mean rotation rate (Figure 4b). Our measurements are consistent with a rotation rate that is inversely proportional to faulted layer thickness as in the simple elastic and pseudoplastic model. In general, our numerically determined rotation rates tend to plot between the average rotation rates predicted for an infinitely strong layer and a pseudoplastic layer with $H_{eff}/H = 0.5$.

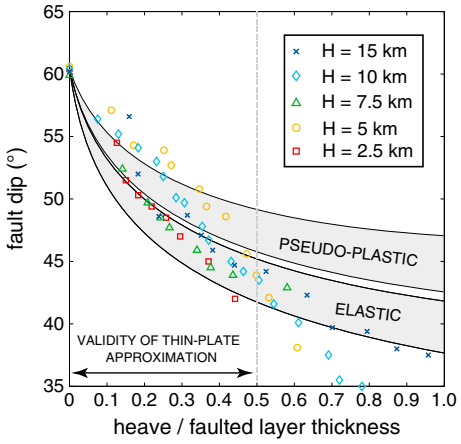

Figure 9. Dip evolution of a normal fault cutting through elastic, pseudoplastic ($H_{eff}/H = 0.5$), and elastoplastic (colored symbols) brittle layers of varying thickness H between 15 and 5 km (The gray area represents the corresponding range of dips.).

5. Discussion

5.1. Work Minimization and Dip Evolution

The models presented in this study illustrate that normal faults rotate in response to the flexure they induce in the surrounding elastic or elastoplastic brittle layer. Complex numerical simulations yield results that are consistent with the assumption that the system evolves along the lowest possible energy path (Figure 3). Consider a fault undergoing a finite amount of horizontal extension Δh.

The associated uplift and subsidence of the footwall and hanging wall will result in (a) accumulation of bending stresses and (b) a moment imbalance that promotes the rotation of the fault toward shallower angles. Growing the fault by Δh while allowing it to rotate by an angle $\Delta\theta$ will result in a smaller increase in fault throw than if the fault were to retain its initial dip. Smaller fault throw means less topographic load on the footwall and hanging wall blocks and therefore a smaller increase in bending work W_{INT} that must be overcome by an increase in the external work W_{EXT}. Rotating the fault by too large an amount, however, will increase the work done by frictional resistance W_{FRIC}, which must also be overcome by W_{EXT}. Therefore, we argue that $\Delta\theta$ adopts the value that optimally balances these two effects. From equation (17) we can see that minimizing the increase in W_{EXT} is equivalent to minimizing the tensional stress σ_R or the tensional force $F_R = H\ \sigma_R$ required to sustain slip on the fault [e.g., *Forsyth*, 1992; *Buck*, 1993]. The first component of W_{EXT} (first term in equation (14)) corresponds to the frictional resistance of the fault and is lowest when $\theta = \theta_0$ immediately after fault initiation ($h = 0^+$). The second component, initially zero (second term in equation (14)), corresponds to the work done by bending the faulted layer and is a growing function of θ (Appendix B). The effect of this term is to shift the minimum in F_R toward smaller dip angles with increasing extension (Figure 3).

We envision several physical mechanisms that can lead to rotation of the active fault plane. The most obvious one is passive advection of the fault in the displacement field induced by continuous flexural readjustment of the footwall and hanging wall blocks. It is unclear, however, whether this effect alone can explain the magnitude and kinetics of rotation observed in our numerical simulations. Another potential mechanism for rotation is that coseismic stress changes during a normal-faulting rupture may induce a net torque about a pivot located near the middle of the faulted layer [*Dempsey et al*., 2012]. In numerical simulations by *Dempsey et al*. [2012], this torque led to finite rotation of the active fault plane over many seismic cycles at rates comparable to those found in this study. In our models we consider continuous slip on a weak fault as opposed to coseismic and interseismic phases. However, it is possible that a similar mechanism may be at play in our simulations, which can be regarded as an extremely slow "coseismic" deformation phase. A third potential mechanism for rotation involves continuous strain relocalization at progressively shallower angles within the narrow weak zone that surrounds a fault in our numerical models. In the Earth, this weak zone could correspond to damage areas that tend to form in the vicinity of faults [e.g., *Collettini*, 2011]. Strain relocalization could be driven by stress rotation due to bending of the footwall and hanging wall. We note that bending of the faulted layer is central to all the mechanisms discussed above, either in terms of displacement field or stress buildup.

We have found that the thickness of the faulted layer, H, exerts the strongest control on the kinematics of flexure-induced fault rotation. This is likely due to the fact that W_{FRIC} scales more strongly with H ($\sim H^2$) than does W_{INT} ($\sim H^{3/2}$ if h is small). We can therefore conclude that in thin layers (small H), the relative increase in W_{EXT} ($= W_{INT} + W_{FRIC}$) corresponding to an increase in fault heave Δh will be comparatively larger and more sensitive to a change in fault dip than in thicker layers. In other words, W_{EXT} will be strongly dependent on the current fault dip if H is small, leading to a larger $\Delta\theta$ for a given Δh. As extension proceeds, topography grows and drives the accumulation of bending stresses. After large amounts of extension, the stress state of the faulted layer is primarily due to the flexure that has already occurred and becomes less and less sensitive to future changes in fault dip, especially when fault heave becomes comparable to the layer thickness. This effect leads to a progressive decrease in rotation rates that is seen both in the semianalytical and numerical models (Figures 4 and 9). The semianalytical models best predict the results of the numerical simulations when fault heave is lower than half of the faulted layer thickness. This could indicate a limitation of the thin plate approximation when fault heave becomes comparable to plate thickness (Figure 9).

5.2. Rheologic Controls on Rotation Rate and Life Span of Normal Faults

The rotation rates we measured in the numerical models (with a realistic treatment of plasticity) agree well with those predicted by our semianalytic work minimization model. Specifically, they tend to plot between the infinitely strong layer (elastic) end-member and a pseudoplastic end-member where the effective elastic thickness is decreased to approximately half the true thickness throughout the layer (Figure 4b). This is consistent with the fact that only a portion of the faulted layer yields in the numerical simulations. Indeed, nonrecoverable deformation accumulates preferentially in a distributed (i.e., nonlocalized manner) regions of high plate curvature [*Bodine and Watts*, 1979; *Buck*, 1988].

The yield stress of the layer acts as an upper bound on the buildup of bending stresses and limits the increase of σ_R [*Buck*, 1993]. Less rotation is therefore required to adjust to the flexural stresses, accounting for slower fault rotation in elastoplastic layers than in purely elastic layers. As fault heave approaches and exceeds H, the bending stress likely saturates over a large enough region that most of the subsequent deflection occurs through plastic flow. This phenomenon is thought to shape the domal morphology of exposed detachment surfaces by "rollover" [*Buck*, 1988; *Lavier et al*., 1999]. If the bending stresses surrounding the fault are fixed at the yield stress, then changes in fault dip will not strongly affect σ_R and the fault will remain stuck at the dip it has reached through past elastoplastic flexure. The numerical simulations of *Choi and Buck* [2012] showed this kind of behavior when fault heave greatly exceeded H. Namely, they found that when the top of the active fault surface had rotated by ~20° from its initiation angle, the fault had reached a near–steady state geometry. *Choi and Buck* [2012] were also able to resolve depth-dependent rotation of the fault zone, with little to no rotation occurring at the base of the fault. Our semianalytical model averages the lithostatic stress along a planar fault zone and thus cannot account for depth-dependent rotation. However, if one replaces $H/2$ by depth along the fault in the derivation of the semianalytical model, one would indeed expect faster fault rotation at shallower depths and the development of concave-down faults at very large offsets.

Fault rotation acts in the same manner as plasticity in limiting the increase in bending stresses during fault growth. *Buck* [1993] quantified the effect of plasticity alone and showed that the maximum flexural stress in an elastoplastic layer scales linearly with H. Specifically, he showed that a fault will grow indefinitely while retaining its dip if the layer is thin enough that σ_R saturates at a value smaller than the stress needed to break a new fault (equation (18)). *Lavier and Buck* [2002] showed that rift zones dominated by long-lived normal faults (e.g., oceanic detachments or metamorphic core complexes) are generally associated with thinner lithosphere than rifts dominated by shorter-lived "half-graben" style faults. Incorporating our mechanism for fault rotation yields a similar prediction to that of a normal fault with constant dip in an extending elastoplastic layer, namely, in both cases infinite fault growth is permitted in thin enough lithosphere. However, the additional influence of fault rotation will allow sustained slip on normal faults formed in thicker lithosphere than would be permitted if fault dip remained fixed at high angle. This is consistent with previous numerical simulations of fault development at mid-ocean ridges by *Behn and Ito* [2008], who found that a force balance model could only predict fault life span in an elastoplastic lithosphere if it incorporated the reduction in fault dip observed in their numerical simulations. This suggests that both the finite yield strength of the lithosphere and the flexural rotation mechanism presented here are important components to the physics of normal fault growth.

The brittle-ductile transition (BDT), which controls the thickness of the layer affected by faulting, is largely thermally controlled and has been inferred to correspond to temperatures of 400–600°C in the oceanic and upper continental crust [e.g., *Hirth et al*., 1998]. The depth, geometry, and evolution of the BDT result from a competition between heat advection in the solid flow field (underlying ductile flow, overlying brittle deformation, and associated uplift/subsidence) and heat conduction, which can be enhanced by hydrothermal processes [*Phipps Morgan and Chen*, 1993; *Lavier and Buck*, 2002]. For simplicity, the numerical simulations presented here do not account for temperature evolution and temperature-dependent rheology. Consequently, the distribution of brittle and ductile materials is solely controlled by advection in the fault-related velocity field. This corresponds to an end-member scenario in which heat conduction and hydrothermal circulation are inefficient at extracting heat from the base of the faulted layer, resulting in a sharp BDT that is offset by the fault. In this scenario the area of contact between the hanging wall and footwall blocks and the thickness of the rock column overlying the fault decreases with increasing fault offset (Figure 10a). Alternatively, if hydrothermal cooling is efficient at extracting heat from the lithosphere, the BDT may remain relatively flat and not mimic the surface topography [e.g., *Lavier and Buck*, 2002], which will in turn result in a smaller reduction in the area of contact during extension.

To investigate whether such changes in the morphology of the BDT will influence the kinematics of fault rotation, we ran numerical simulations of fault growth in elastoplastic lithosphere with a BDT that was forced to remain flat and at a fixed depth (Figure 10b). These runs yielded very similar rotation kinematics to the reference runs presented in Figure 9. The reason for this is twofold. First, bending of the brittle layer affects an area over which the layer thickness is largely unchanged (over a flexural wavelength α), but that is much larger than the zone immediately affected by the fault, making flexural rotation relatively insensitive to a net decrease in layer thickness close to the fault. Second, our model assumes the same density for the faulted

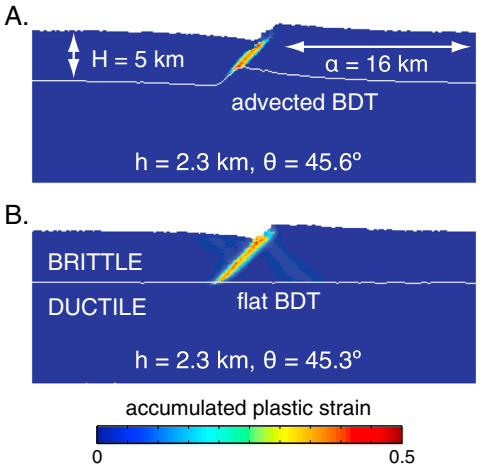

Figure 10. Snapshots of accumulated plastic strain after 2.3 km of horizontal extension along a fault cutting through a 5 km thick elastoplastic layer. (a) The brittle-ductile transition (BDT, white line) is advected in the ambient solid flow field and therefore offset by the fault. (b) The BDT is constrained to remain at a fixed depth, representing a scenario where heat is efficiently extracted through the brittle layer. Evolution of the BDT does not appear to strongly control the rotation kinematics of the fault.

layer and the underlying ductile asthenosphere. This means that gravitational deflection of the lithosphere is solely controlled by the density contrast at the surface/seafloor and is insensitive to the geometry of the BDT. Introducing a buoyancy contrast along the BDT could introduce a restoring load that limits deflection and introduces asymmetry between the footwall and hanging wall [*Weissel and Karner*, 1989], potentially affecting fault rotation.

It is generally thought that fault zones progressively weaken as they accumulate offset, due to effects such as progressive damage and/or precipitation of soft minerals. In our models the fault is systematically treated as a zone of very low cohesion ($<<$ 1 MPa). The choice of a low fault zone cohesion, C, has little effect on the evolution of σ_R, given that $C << \mu\rho gH/2$ in the expression of W_{FRIC} (equation (7)). By contrast, cohesion of the unfaulted brittle material is critical in controlling when a new fault breaks and the previous fault is abandoned (equation (18)). Fault friction, however, has a very strong control on the initiation angle of normal faults (equation (16)). To estimate the extent to which the friction coefficient influences fault rotation, we calculated the dip evolution of low-friction faults using our semianalytical model. We found that fault friction had very little influence on rotation rates (Figure 5b). This is consistent with our interpretation of rotation kinematics being controlled primarily by flexural processes. Fault friction does, however, control the range of angles that an active fault will reach because it controls the angle of fault initiation. If flexure of the brittle layer can account for ~30° of fault rotation over a total extension of ~ H, then a low-friction fault may reach angles as low as 20° if it initiated at 50° ($\mu = 0.2$). An important consequence of this result is that a seismically active normal fault dipping at an angle of 40° could either be a strong ($\mu = 0.6$) fault that has accommodated a significant amount of extension (~30% of the faulted layer thickness) or a weak ($\mu < 0.3$), young normal fault that has accommodated little offset (Figure 5b). While the distinction may be straightforward in the field, it is not at all obvious when one only considers catalogs of normal-faulting earthquakes.

5.3. Implications for Extensional Rift Systems

We propose that the dip distribution of normal-faulting earthquakes (Figure 1) observed both globally and at individual rifts reflects a ubiquitous process of faults initiating at a steep angle (~60°) before rapidly rotating toward shallower dips and being abandoned in favor of a new steep fault. In the framework of our model, the 30–60° range is a reflection of the typical brittle layer thickness (≤ ~15 km) inferred in most extensional settings [e.g., *Chen and Molnar*, 1983]. Indeed, a 15 km brittle layer is thin enough to allow large amounts of rotation over the life span of the fault (Figure 6). If fault segments evolve in relative independence along the axis of a rift, then our model predicts that intermediate- to shallow-dipping faults should be more prevalent than steep faults, consistent with the high-angle tail in the global distribution (Figure 1). Of course, the extent to which the dip evolution of a single normal fault (Figure 5) is reflected in the shape of the global earthquake dip distribution is not straightforward. It depends on (1) the distribution of heaves within a fault population, which reflects the relative timing of fault growth (e.g., sequential versus simultaneous) as well as the degree of along-axis fault interaction and (2) how earthquakes sample the true dip distribution. Indeed, *Wernicke* [1995] suggested that low-angle fault planes may be characterized by longer earthquake recurrence time and therefore be undersampled in global dip catalogs, thereby explaining the low-angle tail and bell shape of the distribution shown in Figure 1.

Our model makes predictions for fault evolution, which can be tested with detailed regional studies of fault geometry and lithospheric rheology. For instance, our model predicts that strong faults ($\mu > 0.6$), which

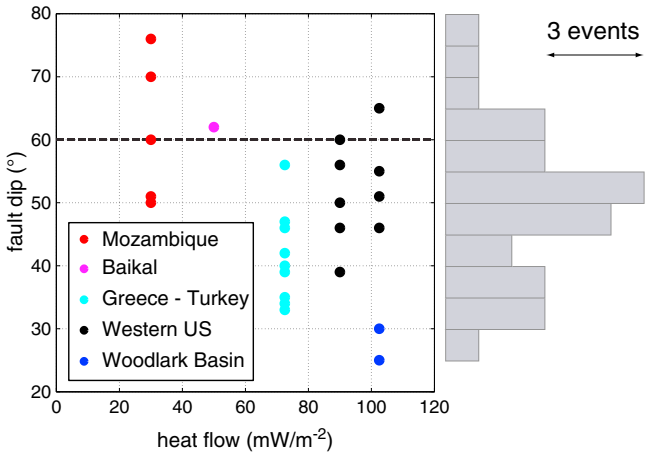

Figure 11. Compilation of normal fault dips making up the distribution shown in Figure 1 plotted against regional heat flow data [*Pollack et al.*, 1993; *Lavier and Buck*, 2002]. Heat flow serves as a proxy for faulted layer thickness, with higher heat flow expected in regions of thinner brittle layers. The global distribution of fault dips is reported on the right side of the graph.

initiate at a steep angle in a thick brittle layer ($H > 25$ km), will only remain active over a few kilometers of extension before they are abandoned in favor of a new fault. Over their short life span, these faults will not experience large rotations from their initiation angle. This is consistent with the steepest-dipping normal-faulting ruptures recorded in Mozambique (51–76° during the 2006 seismic sequence) [*Yang and Chen*, 2008] where the seismogenic layer thickness (~30 km) is notably thicker than is typical in most continental rifts [*Chen and Molnar*, 1983]. Our model suggests that similar steep (slowly rotating) faults should be prevalent in regions of high brittle layer thickness such as the Baikal Rift in central Asia [e.g., *Watts and Burov*, 2003]. Unfortunately, there is not a sufficiently complete record of normal-faulting tensor solutions in which the fault plane can be clearly identified to accurately sample the dip distribution in such settings. Future studies should focus on assembling such detailed catalogs on the regional scale in order to systematically constrain fault dip as a function of lithospheric thickness (e.g., seismogenic layer thickness, equivalent elastic thickness, and thermal models). As a first step in this direction, we compiled representative heat flow measurements for each region present in the global dip distribution shown in Figure 1, using data from the global heat flow data set [*Pollack et al.*, 1993] and the compilation used in *Lavier and Buck* [2002]. We treat conductive heat flow as a proxy for brittle layer thickness, with the expectation of greater heat flow in regions of thinner lithosphere. Figure 11 shows event dip plotted against regional heat flow. Events from Mozambique and the Baikal Rift plot at the high-dip/low-heat flow end. Events from the Woodlark Basin, which are to date the shallowest-dipping normal-faulting ruptures on record, plot on the high heat flux end, which is consistent with our results. Specifically, we expect that the lowest dip that a normal fault can reach should be smaller in thinner faulted layers. If this is the case, thorough regional compilations of unambiguous fault dips may help outline a minimum dip "envelop" on a plot of dip versus heat flow (or another proxy for H).

Another obvious step in testing the predictions of fault rotation made here are through detailed geologic studies using paleomagnetism, thermobarometry, and/or synkinematic sediment sequences to reconstruct the rotational and growth history of normal fault systems. In practice, comparing model predictions of dip versus heave with individual real-world faults is very challenging. This is mainly because measuring the total amount of extension accommodated by a fault is not straightforward, especially if surface processes alter or erase the geomorphological markers of finite extension (e.g., erosion of the uplifting footwall). An additional complication is that surface processes may influence the force balance on a growing normal fault, either by adding load (deposition of sediments on the subsiding hanging wall) and/or by removing/redistributing load through footwall erosion, which would feedback onto the topographic and bending stresses. In the numerical models of *Choi and Buck* [2012], incorporating basin infill on the hanging wall side of a growing fault indeed results in faster and overall greater amounts of fault rotation. Quantifying the effect of such processes on the buildup of flexural stresses and the subsequent readjustment of normal faults is beyond the scope of this study but would constitute an interesting next step with potential implications for tectono-climatic interactions.

Finally, we emphasize that the models presented here are generally well suited for mid-ocean ridge settings. We have considered an end-member of rifting where a single normal fault dominates the strain field, which is often the case at asymmetric mid-ocean ridge segments where long-lived detachments accommodate most of the tectonic extension [*Escartin et al.*, 2008]. Our model predicts that very large offset ($h > H$) detachment faults displaying flat, domal footwalls should dip at a relatively shallow angle (<45°) where they root at the ridge axis. The subsurface geometry of oceanic detachments is still a matter of debate, and to date the only direct constraint

is from a single microseismicity study at the TAG segment of the Mid-Atlantic Ridge [*DeMartin et al.*, 2007]. Their study argues for a shallow-dipping exhumed fault surface that roots into a steep (~70°) active fault. In the conceptual framework of our model, this would only be possible in an extremely weak elastoplastic lithosphere, where rollover of the footwall occurs through widespread plastic flow, and there is limited stress buildup to drive significant rotation of the active fault. Another possibility is that fault rotation is strongly depth dependent and leads to a concave-down fault that retained a steep dip at depth while its upper portion rotated by 20° or more.

It is noteworthy, however, that TAG does not feature a fully formed, corrugated oceanic core complex and has only accommodated about 4 km of horizontal extension between termination and breakaway. It is also unclear whether the steep cluster of seismicity observed at the axis is actually linked to the exhumed fault surface or whether it constitutes the initiation of a new fault at a high angle that marks the recent abandonment of the older TAG fault.

Additional studies of detachment microseismicity are needed to resolve the debate on active detachment roots, which has strong implications on the total amount of rotation recorded by exhumed lower crustal units in the footwall of oceanic core complexes. We propose that footwall rotation recorded by paleomagnetic tracers [e.g., *Garcés and Gee*, 2007; *MacLeod et al.*, 2011] may record both rollover of the exhumed footwall [*Buck*, 1988; *Lavier et al.*, 1999] and rotation of the active fault plane explored in this study. While these two components may be of similar magnitude, we expect rotation of the active fault plane to occur immediately after fault initiation and therefore to be recorded in units closest to the detachment breakaway.

6. Conclusion

We have showed that fault rotation in response to the evolving stress field associated with plate flexure provides a mechanism to explain the distribution of active normal fault dips observed globally and at the scale of individual rift systems. In our model, the fastest rotation rates occur immediately following fault initiation, and the average rotation rates scale as the inverse of the faulted layer thickness. Predicted fault dips span the entire 30–60° dip range documented in earthquake catalogs, except in cases where the faulted layer is > 25 km, in which case it rapidly becomes easier to initiate a new fault than to continue extension and rotation of the active fault. The predictions of our model can be tested through careful regional compilations of normal-faulting mechanisms where one of the two nodal planes can be clearly identified as the rupture plane. Such compilations should be complemented by independent estimates of the thickness of the faulted layer and more generally of the local strength profile of the lithosphere. Fault-induced flexure and topographic stresses are essential controls on fault dip, which must be considered alongside fault strength and faulted layer strength. Finally, the sensitivity of topographic and bending stresses to surface processes (e.g., erosion and deposition) opens a range of implications for the long-term evolution and short-term seismogenic behavior of normal fault systems.

Appendix A: Calculation of the Bending Work Term W_{INT}

To estimate the mechanical work required to bend the faulted layer, W_{INT}, from equation (9), we first calculate the deflection of the faulted layer $w(x)$ due to finite extension on the fault. This is done by convolving the right-hand side of equation (9) with the Green's function describing the response of an infinite elastic thin plate to a point load:

$$w(x) = \int_{-\infty}^{+\infty} G(x,s)(-\Delta\rho g w^*(s))\mathrm{d}s \tag{A1}$$

where $G(x,s)$ is written [*Turcotte and Schubert*, 2002]

$$G(x,s) = \frac{\alpha^3}{8D}\exp\left(-\left|\frac{x-s}{\alpha}\right|\right)\left(\cos\left|\frac{x-s}{\alpha}\right| + \sin\left|\frac{x-s}{\alpha}\right|\right) \tag{A2}$$

and $w^*(x)$ is defined as

$$w^*(x) = \begin{cases} -\frac{h}{2}\tan\theta, \forall x < -\frac{h}{2} \\ x\tan\theta, \forall x \in \left[-\frac{h}{2}, \frac{h}{2}\right] \\ +\frac{h}{2}\tan\theta, \forall x > +\frac{h}{2} \end{cases} \tag{A3}$$

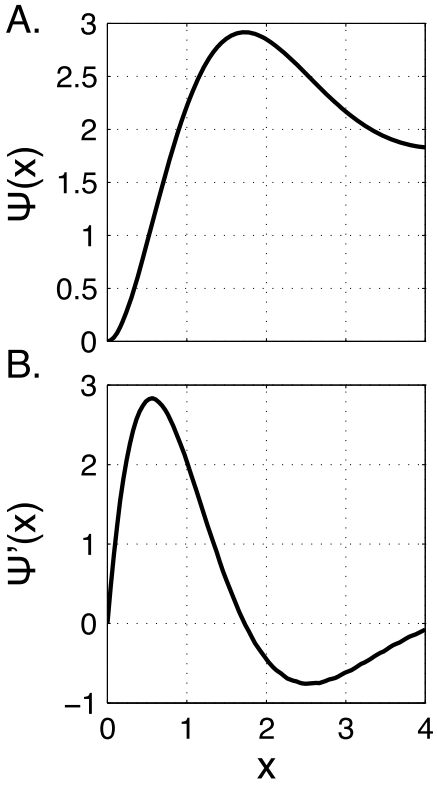

Figure A1. Graphical representation of (a) dimensionless function $\Psi(x)$ and (b) its first derivative. $\Psi(x)$ is used in the calculation of W_{INT} (equation (12)), and $\Psi'(x)$ is used in the calculation of σ_R through equation (B12).

This yields the total fault-induced topography $w^T(x) = w(x) + w^*(x)$

$$w^T(x) = \frac{1}{4}\alpha\tan\theta\left(f\left(\left|\frac{x-h/2}{\alpha}\right|\right) - f\left(\left|\frac{x+h/2}{\alpha}\right|\right)\right) \quad \text{(A4)}$$

where $f(x)$ is a dimensionless function defined as

$$f(x) = \exp(-x)(\sin x - \cos x) \quad \text{(A5)}$$

From equation (9), we can now write

$$W_{INT} = \frac{D}{16\alpha^2}\tan^2\theta\int_0^{+\infty}\left(f''\left(\left|\frac{x-h/2}{\alpha}\right|\right) - f''\left(\left|\frac{x+h/2}{\alpha}\right|\right)\right)^2 dx \quad \text{(A6)}$$

which can also be expressed as

$$W_{INT} = \frac{D}{16\alpha}\tan^2\theta\,\Psi\left(\frac{h}{\alpha}\right) \quad \text{(A7)}$$

Where $\Psi(y)$ is related to $f(x)$ by

$$\Psi(y) = \int_0^{+\infty}\left(f''\left(\left|x-\frac{1}{2}y\right|\right) - f''\left(\left|x+\frac{1}{2}y\right|\right)\right)^2 dx \quad \text{(A8)}$$

The function $\Psi(y)$ is estimated numerically with the trapezoidal method. Its graphical representation is shown in Figure A1a.

Appendix B: Equations for Fault Dip, Work, and Stress as a Function of Heave

Each term in equation (14), W_{FRIC} and W_{INT}, can be written as the product of a function of dip, $A(\theta)$, and a function of heave, $R(h)$. Specifically,

$$A_F(\theta) = \frac{1}{\sin\theta\cos\theta + \mu\sin^2\theta} \quad \text{(B1)}$$

$$R_F(h) = (C + \mu\rho gH/2)Hh \quad \text{(B2)}$$

$$A_I(\theta) = \tan^2\theta \quad \text{(B3)}$$

$$R_I(h) = \frac{D}{16\alpha}\Psi\left(\frac{h}{\alpha}\right) \quad \text{(B4)}$$

To determine the fault dip that minimizes the increase in total extensional work (W_{EXT}) with increasing extension, we differentiate W_{EXT} with respect to h and θ:

$$\frac{\partial}{\partial\theta}\left(\frac{\partial W_{EXT}}{\partial h}\right) = (A_F''(\theta)R_F(h) + A_F''(\theta)R_F(h))\frac{\partial\theta}{\partial h} + A_F'(\theta)R_F'(h) + A_I'(\theta)R_I'(h) \quad \text{(B5)}$$

and this equal to zero to obtain the following nonlinear ordinary differential equation:

$$\frac{\partial\theta}{\partial h} = -\frac{A_F'(\theta)R_F'(h) + A_I'(\theta)R_I'(h)}{A_F''(\theta)R_F(h) + A_I''(\theta)R_I(h)} \quad \text{(B6)}$$

Equation (B6) is solved with a fourth-order Runge-Kutta method with the initial condition $\theta(h=0) = \theta_0$. Below are the expressions of the first- and second-order derivatives of functions A and R.

$$A_F'(\theta) = -\frac{\csc^4\theta(\cos 2\theta + \mu\sin 2\theta)}{(\mu + \cot\theta)^2} \quad \text{(B7)}$$

$$A_F''(\theta) = \frac{2\csc^2\theta}{(\mu + \cot\theta)^3}\left(1 + \mu^2 + 3\mu^2\cot^2\theta + 3\mu\cot^3\theta - \mu\cot\theta + \cot^4\theta\right) \quad \text{(B8)}$$

$$A_l'(\theta) = 2\tan\theta\sec^2\theta \tag{B9}$$

$$A_l''(\theta) = -2(\cos 2\theta - 2)\sec^4\theta \tag{B10}$$

$$R_F'(h) = (C + \mu\rho g h/2)H \tag{B11}$$

$$R_l'(h) = \frac{D}{16\alpha^2}\Psi'\left(\frac{h}{\alpha}\right) \tag{B12}$$

The graphical representation of $\Psi'(x)$ (estimated numerically) is shown in Figure A1b.

Acknowledgments
The authors wish to thank Jean-Philippe Avouac, Roger Buck, Javier Escartin, Don Forsyth, Garrett Ito, and Eric Mittelstaedt for fruitful discussions. This work was supported by NSF grants OCE-1154238 and EAR-1010432.

References

Abers, G. A. (1991), Possible seismogenic shallow-dipping normal faults in the Woodlark-D'Entrecasteaux extensional province, Papua New Guinea, *Geology*, *19*, 1205–1208.

Abers, G. A., C. Z. Mutter, and J. Fang (1997), Shallow dips of normal faults during rapid extension: Earthquakes in the Woodlark-D'Entrecasteaux rift system, Papua New Guinea, *J. Geophys. Res.*, *102*, 15,301–15,317, doi:10.1029/97JB00787.

Anderson, E. M. (1951), *The Dynamics of Faulting*, 2nd ed., Oliver and Boyd, Edinburgh, U. K.

Behn, M. D., and G. Ito (2008), Magmatic and tectonic extension at mid-ocean ridges: 1. Controls on fault characteristics, *Geochem. Geophys. Geosyst.*, *9*, Q08O10, doi:10.1029/2008GC001965.

Bodine, J. H., and A. B. Watts (1979), On lithospheric flexure seaward of the Bonin and Mariana trenches, *Earth Planet. Sci. Lett.*, *43*(1), 132–148.

Buck, W. R. (1988), Flexural rotation of normal faults, *Tectonics*, *7*(5), 959–973, doi:10.1029/TC007i005p00959.

Buck, W. R. (1993), Effect of lithospheric thickness on the formation of high- and low-angle normal faults, *Geology*, *21*(10), 933–936, doi:10.1130/00917613(1993)021<0933:EOLTOT>2.3.CO;2.

Byerlee, J. (1978), Friction of rocks, *Pure Appl. Geophys.*, *116*(4–5), 615–626, doi:10.1007/BF00876528.

Chen, W.-P., and P. Molnar (1983), Focal depths of intracontinental and intraplate earthquakes and their implications for the thermal and mechanical properties of the lithosphere, *J. Geophys. Res.*, *88*(B5), 4183–4214, doi:10.1029/JB088iB05p04183.

Choi, E., and W. R. Buck (2012), Constraints on the strength of faults from the geometry of rider blocks in continental and oceanic core complexes, *J. Geophys. Res.*, *117*, B04410, doi:10.1029/2011JB008741.

Collettini, C. (2011), The mechanical paradox of low-angle normal faults: Current understanding and open questions, *Tectonophysics*, *510*, 253–268, doi:10.1016/j.tecto.2011.07.015.

Collettini, C., and R. H. Sibson (2001), Normal faults, normal friction?, *Geology*, *29*(10), 927–930, doi:10.1130/0091-7613(2001)029<0927:NFNF>2.0.CO;2.

Cooke, M. L., and S. Murphy (2004), Assessing the work budget and efficiency of fault systems using mechanical models, *J. Geophys. Res.*, *109*, B10408, doi:10.1029/2004JB002968.

Crameri, F., H. Schmeling, G. J. Golabek, T. Duretz, R. Orendt, S. J. H. Buiter, D. A. May, B. J. P. Kaus, T. V. Gerya, and P. J. Tackley (2012), A comparison of numerical surface topography calculations in geodynamic modelling: An evaluation of the "sticky air" method, *Geophys. J. Int.*, *189*, 38–54, doi:10.1111/j.1365-246X.2012.05388.x.

DeMartin, B. J., R. A. Sohn, J. P. Canales, and S. E. Humphris (2007), Kinematics and geometry of active detachment faulting beneath the Trans-Atlantic Geotraverse (TAG) hydrothermal field on the Mid-Atlantic Ridge, *Geology*, *35*, 711–714, doi:10.1130/G23718A.1.

Dempsey, D. E., S. M. Ellis, J. V. Rowland, and R. A. Archer (2012), The role of frictional plasticity in the evolution of normal fault systems, *J. Struct. Geol.*, *39*, 122–137, doi:10.1016/j.jsg.2012.03.001.

Escartin, J., G. Hirth, and B. Evans (1997), Effects of serpentinization on the lithospheric strength and the style of normal faulting at slow-spreading ridges, *Earth Planet. Sci. Lett.*, *151*(3–4), 181–189, doi:10.1016/S0012-821X(97)81847-X.

Escartin, J., D. K. Smith, J. Cann, H. Schouten, C. H. Langmuir, and S. Escrig (2008), Central role of detachment faults in accretion of slow-spreading oceanic lithosphere, *Nature*, *455*, 790–794, doi:10.1038/nature07333.

Forsyth, D. W. (1992), Finite extension and low-angle normal faulting, *Geology*, *20*(1), 27–30, doi:10.1130/0091-7613(1992)020<0027:FEALAN>2.3.CO;2.

Garcés, M., and J. S. Gee (2007), Paleomagnetic evidence of large footwall rotations associated with low-angle faults at the Mid-Atlantic Ridge, *Geology*, *35*, 279–282, doi:10.1130/G23165A.

Gerya, T. (2010), *Introduction to Numerical Geodynamic Modelling*, Cambridge Univ. Press, Cambridge, U. K.

Harlow, F. H., and J. E. Welch (1965), Numerical calculation of time-dependent viscous incompressible flow of fluid with free surface, *Phys. Fluids*, *8*(12), 2182–2189, doi:10.1063/1.1761178.

Hirth, G., J. Escartín, and J. Lin (1998), The rheology of the lower oceanic crust: Implications for lithospheric deformation at mid-ocean ridges, in *Faulting and Magmatism at Mid-Ocean Ridges*, *Geophys. Monogr. Ser.*, vol. 106, edited by W. R. Buck et al., pp. 291–303, AGU, Washington, D. C., doi:10.1029/GM106p0291.

Jackson, J. A., and N. J. White (1989), Normal faulting in the upper continental crust: Observations from regions of active extension, *J. Struct. Geol.*, *11*(1–2), 15–36, doi:10.1016/0191-8141(89)90033-3.

King, G. C. P., R. S. Stein, and J. B. Rundle (1988), The growth of geological structures by repeated earthquakes: 1. Conceptual framework, *J. Geophys. Res.*, *93*(B11), 13,307–13,318, doi:10.1029/JB093iB11p13307.

Lavier, L. L., and W. R. Buck (2002), Half graben versus large-offset low-angle normal fault: Importance of keeping cool during normal faulting, *J. Geophys. Res.*, *107*(B6), doi:10.1029/2001JB000513.

Lavier, L. L., W. R. Buck, and A. N. B. Poliakov (1999), Self-consistent rolling-hinge model for the evolution of large-offset low-angle faults, *Geology*, *27*(12), 1127–1130, doi:10.1130/0091-7613(1999)027<1127:SCRHMF>2.3.CO;2.

Lavier, L. L., W. R. Buck, and A. N. B. Poliakov (2000), Factors controlling normal fault offset in an ideal brittle layer, *J. Geophys. Res.*, *105*(B10), 23,431–23,442, doi:10.1029/2000JB900108.

MacLeod, C. J., J. Carlut, J. Escartin, H. Horen, and A. Morris (2011), Quantitative constraint on footwall rotations at the 15°45'N oceanic core complex, Mid-Atlantic Ridge: Implications for oceanic detachment fault processes, *Geochem. Geophys. Geosyst.*, *12*, Q0AG03, doi:10.1029/2011GC003503.

Moresi, L., F. Dufour, and H.-B. Muhlhaus (2003), Lagrangian integration point finite element method for large deformation modeling of viscoelastic geomaterials, *J. Comput. Phys.*, *184*, 476–497.

Phipps Morgan, J., and Y. J. Chen (1993), The genesis of oceanic crust: Magma injection, hydrothermal circulation, and crustal flow, *J. Geophys. Res.*, *98*(B4), 6283–6297, doi:10.1029/92JB02650.

Pollack, H. N., S. J. Hurter, and J. R. Johnson (1993), Heat flow from the Earth's interior: Analysis of the global data set, *Rev. Geophys.*, *31*(3), 267–280.

Proffett, J. M. (1977), Cenozoic geology of the Yerington district, Nevada, and implications for the nature and origin of Basin and Range faulting, *Bull. Geol. Soc. Am.*, *88*(2), 247–266, doi:10.1130/0016-7606(1977)88<247:CGOTYD>2.0.CO;2.

Shaw, W. J., and J. Lin (1996), Models of ocean ridge lithospheric deformation: Dependence on crustal thickness, spreading rate, and segmentation, *J. Geophys. Res.*, *101*(B8), 17,977–17,993, doi:10.1029/96JB00949.

Spencer, J. E., and C. G. Chase (1989), Role of crustal flexure in initiation of low-angle normal faults and implications for structural evolution of the basin and range province, *J. Geophys. Res.*, *94*(B2), 1765–1775, doi:10.1029/JB094iB02p01765.

Thatcher, W., and D. P. Hill (1991), Fault orientations in extensional and conjugate strike-slip environments and their implications, *Geology*, *19*(11), 1116–1120, doi:10.1130/0091-7613(1991)019<1116:FOIEAC>2.3.CO;2.

Turcotte, D. L., and G. Schubert (2002), *Geodynamics*, 2nd ed., Cambridge Univ. Press, Cambridge, U. K.

Vening-Meinesz, F. A. (1950), Les grabens Africains résultants de compression ou de tension de la croûte terrestre?, *Bull. Inst. R. Colon. Belg.*, *21*, 539–552.

Watts, A. B., and E. B. Burov (2003), Lithospheric strength and its relationship to the elastic and seismogenic layer thickness, *Earth Planet. Sci. Lett.*, *213*, 113–131, doi:10.1016/S0012-821X(03)00289-9.

Weissel, J. K., and G. D. Karner (1989), Flexural uplift of rift flanks due to mechanical unloading of the lithosphere during extension, *J. Geophys. Res.*, *94*(B10), 13,919–13,950, doi:10.1029/JB094iB10p13919.

Wernicke, B. (1995), Low-angle normal faults and seismicity: A review, *J. Geophys. Res.*, *100*(B10), 20,159–20,174, doi:10.1029/95JB01911.

Wernicke, B., and G. J. Axen (1988), On the role of isostasy in the evolution of normal fault systems, *Geology*, *16*(9), 848–851, doi:10.1130/00917613(1988)016<0848:OTROII>2.3.CO;2.

Yang, Z., and W.-P. Chen (2008), Mozambique earthquake sequence of 2006: High-angle normal faulting in southern Africa, *J. Geophys. Res.*, *113*, B12303, doi:10.1029/2007JB005419.